skb.se

SKB P-22-20

ISSN 1651-4416

ID 1995098

November 2022

EBS TF – THM modelling

Water transport in pellets-filled slots – modelling of Subtask B

Ola Kristensson, Daniel Malmberg
Clay Technology AB

Mattias Åkesson
Svensk Kärnbränslehantering AB

Keywords: Water transport, Piping, Bentonite, Pellet filling, Simulation, Comsol

Abstract

This report describes the work undertaken within the Task Force on Engineered Barrier Systems when developing a model capable of simulating water transport in pellet-filled slots. The case which has been addressed is that of Subtask B within Task 10, where water is added as a point inflow and with a constant inflow rate. One particular feature of the model is the capability to develop highly permeable piping channels. The model was implemented in Comsol Multiphysics where the possibility to formulate partial differential equations and incorporate state variables was used.

The model shows capabilities of developing piping channels and give different water saturation patterns for different water inflow rates, something also observed experimentally. There is, however, some error in the implementation regarding the determination of the channel segment orientation which has to be taken care of before further use of the model.

Sammanfattning

Denna rapport beskriver arbetet utfört inom ”Task Force on Engineered Barrier Systems” med att utveckla en modell där vattenflöde i pelletsfyllda spalter kan representeras. Det fall som studerats är ”Subtask” B inom Uppgift 10 där vatten tillsätts som ett konstant punktinflöde. En speciell egenskap hos modellen är att den kan representera uppkomsten av öppna kanaler. Modellen implementerades i Comsol Multiphysics där möjligheten att formulera partiella differentialekvationer och använda sig av tillståndsvariabler utnyttjades.

I modellen kan kanalbildning ske och olika vattenupptagstransportmönster bildas vid olika inflödeshastigheter, vilket också har observerats i experiment. Det är emellertid något fel i implementeringen vad gäller orienteringen av de nybildade kanalsegmenten, vilket måste åtgärdas innan fortsatt användning av modellen.

Content

1 Introduction

The work reported here concerns Task 10, “Water transport in pellet-filled slots”, within the Task Force on Engineered Barrier Systems. Task 10, in turn, had several subtasks, and here work related to subtask B, “Constant water inflow rate from a point inflow”, is reported.

The work presented in this report was carried out as to develop a model capable of capturing different modes of water saturation pattern observed in experiments where water saturation of pellet filled slots were studied, see Börgesson et al. (2015). One particular feature of the model is the ability to develop piping channels where water may flow more easily as compared to the surrounding material. The basis of the model is the structural assumptions considered representative for compacted bentonite which have been used before when developing the HBM-model, see Kristensson et al. (2021), and to this yet a level of pore space, between pellets, has been added.

The report starts with describing the model: the structural assumptions, the balance equations, and the constitutive laws. In the next section the implementation in Comsol Multiphysics is described. Then follows two test simulations, the first evaluating the piping channel formation logic and the second addressing the capability to produce different modes of water saturation patterns for different point inflow rates. Finally, conclusions and comments on the results are given.

2 Theory

Only hydraulic processes are directly simulated in the model. There are, however, underlying mechanical assumptions made when choosing retention curves, such as considering a volume element of the pellet filling mixture as being constant, and prescribing a constant ratio between the so-called macro and meso pore volumes.

This chapter starts with describing the assumed material structure. Thereafter follows a description of the balance equations which in turn is followed by an overview of the used constitutive laws.

2.1 Material structure

When representing a filling with pellets consisting of unsaturated compacted bentonite, yet a level is added to the hierarchy used in previous representations of compacted bentonite blocks, see Figure 2-1. No additional constituents are added, the unsaturated clay system with volume element dv is still considered a mixture of the same three constituents: *minerals*, *water* and dry *air*. It should be noted that the assumptions made regarding which and how the three constituents are mixed in order to define the immiscible phases will not be discussed to begin with, only the more general assumptions regarding the material structure.

Using the information given in Figure 2-1, the relations,

$$dv = dv^{*} + dv^{**} = dv' + dv'' + dv^{**} ,$$

between volume elements can be formulated. The first of the lower-level immiscible phases, in dv', is identical to a saturated material representation. It is in turn a mixture of two immiscible phases with volume elements dv_s and ${}^{\mu}dv_p$, containing solids and fluids, respectively. Thus,

$$dv' = dv_s + {}^{\mu}dv_p ,$$

and the corresponding void ratio and porosity are given by,

$$e_\mu = \frac{dv' - dv_s}{dv_s} \text{ and } \phi_\mu = \frac{dv' - dv_s}{dv'} \text{ ,repectively.}$$

The second of the lower-level immiscible phases, in dv'', is in turn a mixture of fluids occupying the entire volume element and is denoted ${}^{m}dv_p$.

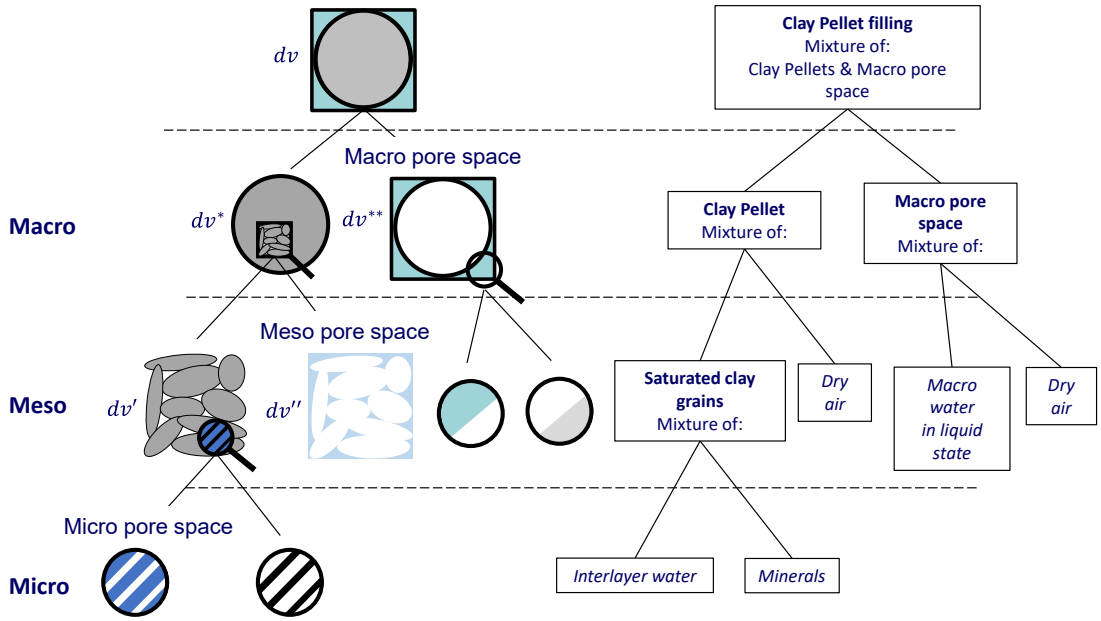

Figure 2-1. Material structure and the constituent map.

For the mixture at the mid-level, in dv^*, the corresponding void ratio and porosity are given by,

$$e_m = \frac{dv^* - dv'}{dv'} \text{ and } \phi_m = \frac{dv^* - dv'}{dv^*} \text{ , repectively.}$$

The second of the mid-level immiscible phases, in dv^{**}, is in turn a mixture of fluids occupying the entire volume element and is denoted ${}^{M}dv_p$.

For the mixture at the highest level, in dv, the corresponding void ratio and porosity are given by,

$$e_M = \frac{dv - dv^*}{dv^*} \text{ and } \phi_M = \frac{dv - dv^*}{dv} \text{ , repectively.}$$

With the total void ratio/porosity defined as,

$$e = \frac{dv - dv_s}{dv_s} \text{ and } \phi = \frac{dv - dv_s}{dv}$$

the following relation holds between the void ratios/porosities,

$$e + 1 = \left(e_\mu + 1\right)(e_m + 1)(e_M + 1) \text{ and } 1 - \phi = \left(1 - \phi_\mu\right)(1 - \phi_m)(1 - \phi_M).$$

Again, the notation using indexes (μ, m and M) indicates that entities belong to pore-spaces at different levels in the hierarchy: microscopic (μ), mesoscopic (m), and macroscopic (M), respectively.

Now, the basic material structure described above is equipped with constituents as shown in Figure 2-1. The case which will be simulated using the model is an isothermal test with a prescribed inflow of water into a pellets filling supported by a confining structure. Water vapor is not included in the model, only water in a liquid state, present on micro (${}^{\mu}dv_l{}^{w}$) and macro scales (${}^{M}dv_l{}^{w}$), is considered. Thus, for the present isothermal case, vapor transport is assumed to have an insignificant effect as compared to the liquid water transport. Micro, meso and macro void ratios can be expressed as:

$$e_\mu = \frac{{}^{\mu}dv_l{}^{w}}{dv_s},$$

$$e_m = \frac{{}^{m}dv_g{}^{a}}{dv_s + {}^{\mu}dv_l{}^{w}},$$

$$e_M = \frac{{}^{M}dv_g{}^{a} + {}^{M}dv_l{}^{w}}{dv_s + {}^{\mu}dv_l{}^{w} + {}^{m}dv_g{}^{a}},$$

where mesoscopic and macroscopic dry air volumes, ${}^{m}dv_g{}^{a}$ and ${}^{M}dv_g{}^{a}$ have been used. Since there are immiscible phases in the formulation it is possible to express some variants of degree of saturation. If defining the total and macro liquid degree of saturations according to,

$$S_l = \frac{dv_l}{dv_p} \text{ and } {}^{M}S_l = \frac{{}^{M}dv_l{}^{w}}{{}^{M}dv_p},$$

respectively, it is possible to derive the expression,

$$S_l = \frac{dv_l}{dv_p} = \frac{{}^{\mu}dv_l{}^{w}}{dv_p} + \frac{{}^{M}dv_l{}^{w}}{dv_p} = \frac{e_\mu}{e} + {}^{M}S_l\frac{\phi_M}{\phi}.$$

In the expression above a total liquid volume, dv_l, and pore volume, dv_p, were introduced.

As mentioned above, it has been assumed that $d\dot{v} = 0$, which gives $\dot{e} = 0$ and $\dot{\phi} = 0$, and it is further assumed that the ratio between the meso and macro pore volumes, β, is constant:

$$\frac{{}^{m}dv_g{}^{a}}{{}^{M}dv_g{}^{a} + {}^{M}dv_l{}^{w}} = \frac{e_m}{e_M}\frac{1}{1 + e_m} = \beta\,.$$

Using this together with the definitions of e_μ, e_m and e_M, and their relation to e and $\dot{e} = 0$ we get:

$$e_m = \frac{\beta}{1+\beta}\left(\frac{e-e_\mu}{1+e_\mu}\right) \rightarrow \dot{e}_m = \frac{-\beta}{1+\beta}\frac{1+e}{\left(1+e_\mu\right)^2}\dot{e}_\mu \,,$$

$$e_M = \frac{e-e_\mu}{(1+e)\beta+1+e_\mu} \rightarrow \dot{e}_M = \frac{-(1+\beta)(1+e)}{\left((1+e)\beta+1+e_\mu\right)^2}\dot{e}_\mu \,.$$

2.2 Balance equations

From the assumed material structure, water mass balance equations,

$$(1-\phi)\dot{\overline{{}^{\mu}\rho_l e_\mu}} + \operatorname{div}\left({}^{\mu}\rho_l\, {}^{\mu}\boldsymbol{q}_l\right) = {}^{\mu}f_l^{\,w} \,,$$

and

$$(1-\phi)\dot{\overline{{}^{M}\rho_l\, {}^{M}S_l e_M(1+e_m)(1+e_\mu)}} + \operatorname{div}\left({}^{M}\rho_l\, {}^{M}\boldsymbol{q}_l\right) = {}^{M}f_l^{\,w} \,,$$

here written separately on micro and macro scales, respectively, can be derived.

The balance equations above include liquid water densities ${}^{\mu}\rho_l$ and ${}^{M}\rho_l$, at the micro and macro scale, Darcy fluxes ${}^{\mu}\boldsymbol{q}_l$ and ${}^{M}\boldsymbol{q}_l$, describing the flow of liquid water through the porous material at the micro and macro scale, a macro degree of water saturation ${}^{M}S_l$, and finally source terms ${}^{\mu}f_l^{\,w}$ and ${}^{M}f_l^{\,w}$ at the micro and macro scale.

Micro and macro suction, s_μ and s_M, respectively, are chosen as the independent variables. The remaining dependent variables to be specified are listed below together with the material characteristic constitutive law from which they are obtained:

${}^{\mu}\rho_l : Water\ density\ in\ pellets$	${}^{\mu}\boldsymbol{q}_l : Darcy\ flow\ in\ the\ clay\ pellets$
${}^{M}\rho_l : Water\ density\ in\ macro\ pores$	${}^{M}\boldsymbol{q}_l : Darcy\ flow\ in\ the\ macro\ pores$
$e_\mu : Retention\ of\ the\ clay\ pellets$	${}^{\mu}f_l^{\,w} : Water\ mass\ transfer\ to\ micro\ pores$
${}^{M}S_l : Retention\ of\ the\ macropores$	${}^{M}f_l^{\,w} : Water\ mass\ transfer\ to\ macro\ pores$

2.3 Constitutive models

For simplicity, equal and constant water densities at the two scales have been assumed,

$${}^{\mu}\rho_l = {}^{M}\rho_l = \rho_l \quad , \rho_l = 1000\ \mathrm{kg/m^3}.$$

The microscopic retention, the retention for the clay pellets, was given by,

$$\frac{e_\mu}{e} = \left(1+\left(\frac{\max(s_\mu,0)}{P_\mu}\right)^{\frac{1}{1-\lambda_\mu}}\right)^{-\lambda_\mu} \quad , P_\mu = 0.4717\ \mathrm{MPa}, \lambda_\mu = 0.25 \,,$$

and its graph is presented in Figure 2-2.

The way of expressing the macroscopic retention, the retention for the pore structure between the pellets, has changed during the model development. To begin with the macroscopic retention curve was defined by,

$${}^{M}S_l = \min\left(1, {}^{M}S_l^{\,ref} + \left(1-{}^{M}S_l^{\,ref}\right)\exp\left(\frac{-\max(s_M,-1000\ \mathrm{Pa})}{P_M}\right)\right),$$

where $P_M = 300$ Pa and ${}^{M}S_l^{\,ref} = 0.01$. This results in a more or less binary function, where the saturation attains either 0.01 or 1, and the suction has an effect when $s_M > -1$ MPa. Using this, however, did not give the sought characteristics of the overall model and therefore the retention curve

described in Eriksson (2020) was tested. This retention curve was formulated by using the Brooks and Cory model as a starting point, where the capillary pressure, p_c, of the considered phase depends on the degree of saturation s_1 of the same phase according to,

$$p_c = P_M \cdot \frac{1}{{s_1}^{1/\lambda_M}}$$

If considering the gas phase in the macro pore system, $p_c = -s_M$ and $s_1 = 1 - {}^M S_l$. If inserting this in the Brooks and Cory model we obtain,

$${}^M S_l = 1 - \left(\frac{-s_M}{P_M}\right)^{-\lambda_M}$$

To avoid negative degree of saturation at $s_M > -p_{ec}$ an alteration of the equation was made as to shift this condition to zero, i.e. ${}^M S_l < 0$ when $s_M > 0$. The final retention, thus intended to work when $s_M < 0$, reads,

$${}^M S_l = 1 - \left(\frac{P_M - s_M}{P_M}\right)^{-\lambda_M} \quad , P_M = 1300 \text{ Pa} \, , \lambda_M = 0.75 \ ,$$

and is graph is shown in Figure 2-2. Since there is no built-in prevention against obtaining positive macro suctions in the formulation presented so far, which would cause an unrealistic degree of saturation in the macro phase, other parts of the formulation must be defined with this in mind. As will be shown below, both relative permeability and water mass transfer coefficients have features that prevent macroscopic water transport when the degree of saturation reach low levels.

For simplicity, the water in the pellets has been assumed to be immobile, i.e.

$${}^\mu \boldsymbol{q}_l = \boldsymbol{0} \, .$$

The water flow in the macro pore structure is described by Darcy's law,

$${}^M \boldsymbol{q}_l = \frac{\boldsymbol{\kappa}}{\mu} (\boldsymbol{\nabla}(s_M) + \rho_l \boldsymbol{g}) \, .$$

$$\mu = 1 \cdot 10^{-3} \text{ Pa} \cdot \text{s}$$

$$\boldsymbol{g} = -9.81 \boldsymbol{e}_z \text{ m/s}^2$$

The permeability $\boldsymbol{\kappa}$ contains an intrinsic permeability, $\boldsymbol{\kappa}_0 = \kappa_0 f(\phi_M)\boldsymbol{1}$, multiplied with a relative permeability $\kappa_{rel} = g({}^M S_l)$. $f(\phi_M)$ and $g({}^M S_l)$ denotes functions of macro porosity and macro saturation, which have changed during the development of the formulation.

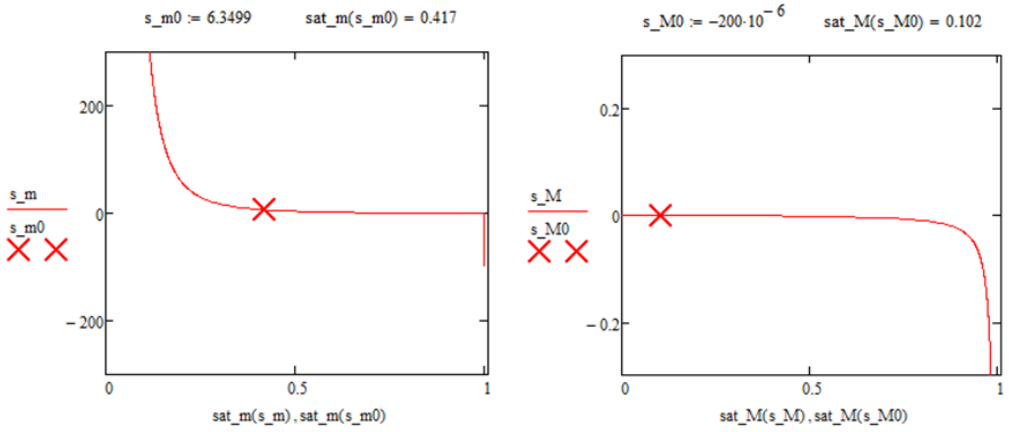

Figure 2-2. Retention curves for the micro scale (left) and macro scale (right).

A Kozeny-Carman model, commonly used when simulating laminar flow through filter beds, was used as a starting point in an early version of the formulation. From the Kozeny-Carman model we may identify,

$$\kappa_0 f(\phi_M) = \frac{d^2}{180}\frac{{\phi_M}^3}{(1-\phi_M)^2},$$

where d denotes the average diameter of the particles in the filter bed. In our case the individual pellets, where $d \approx 1$ cm, are "particles" in the "filter bed", the pellet filling. Since the system we seek to simulate is far from a conventional filter bed it is not surprising that we had to modify the formulation, here by adding a multiplier, $fact_\kappa$, to the expression:

$$\kappa_0 f(\phi_M) = fact_\kappa \frac{d^2}{180}\frac{{\phi_M}^3}{(1-\phi_M)^2}.$$

The value of the introduced multiplier is discussed last in this section. During the development of the material model the porosity dependent function was also changed so that

$$\kappa_0 f(\phi_M) = fact_\kappa \frac{d^2}{180}\frac{{\phi_M}^3}{(1-\phi_M)^2}\frac{\left(1-{\phi_M}^0\right)^2}{\left({\phi_M}^0\right)^3},$$

which we usually use for representing bentonite blocks. In this expression, ${\phi_M}^0$ is the initial macro porosity.

For the relative permeability, represented by the saturation dependent function $g\left({}^M S_l\right)$, a power law was chosen early in the development process, i.e.

$$g\left({}^M S_l\right) = {}^M S_l{}^\beta,$$

where $\beta = 4$ was used. It should be mentioned that the power law was modified to obtain a more numerically convenient formulation both at very low and at very high saturation. When starting to use the new macro retention curve, however, another formulation, which aimed at preventing the macro saturation becoming negative, was formulated. The new relative permeability function reads,

$$g\left({}^M S_l\right) = \frac{1}{1+\exp\left(\frac{a-{}^M S_l}{b}\right)}, a = 0.3, b = 0.03.$$

When the process of pipe formation was included in the formulation, an additional contribution was added to the "standard" permeability in form of a pipe permeability $\boldsymbol{\kappa}_{pipe} = pipe \cdot \kappa_{pipe}\mathbf{1}$. Thus, the total permeability reads,

$$\boldsymbol{\kappa} = \boldsymbol{\kappa}_0 \kappa_{rel} + \boldsymbol{\kappa}_{pipe}.$$

κ_{pipe} denotes a constant additional permeability and $pipe$ denotes a state variable which equals 1 if there is a piping channel at the point or 0 if there is not. The algorithm used to determine the state of $pipe$ is described last in this section. The value used for the piping permeability is,

$$\kappa_{pipe} = 5 \cdot 10^{-13}\ \mathrm{m}^2.$$

The final part of the formulation is to describe water transport between the micro and macro scale. It is expressed using the source terms, ${}^\mu f_l{}^w$ and ${}^M f_l{}^w$, respectively. In order to conserve water mass these two terms should add up to zero. This can be expressed as,

$${}^\mu f_l{}^w = +\dot{\alpha},$$

$${}^M f_l{}^w = -\dot{\alpha},$$

by introducing a variable $\dot{\alpha}$, here defined as water inflow from the macro to the micro scale. The source variable was expressed as a function of micro suction and macroscopic saturation:

$$\dot{\alpha} = \dot{\alpha}_0\ \mathrm{step}\left({}^M S_l - {}^M S_l{}^0\right) s_\mu.$$

In the expression above $\dot{\alpha}_0$ is a constant, the step function, expressed in terms of the macroscopic saturation, acts as to prevent macroscopic saturation becoming negative and micro suction drives water from the macro to the micro level. When initially prescribing the constant $\dot{\alpha}_0$, the rough example that one pellet with a volume of about 1 cm^2 takes up 1 g water in 30 min was used. During test calculations, however, this setup was altered. As in the case of the intrinsic permeability, a multiplier, denoted $fact_\alpha$, was introduced as to obtain,

$$\dot{\alpha}_0 = fact_\alpha \frac{1}{30} \frac{g}{\text{cm}^3 \cdot \text{min}} \frac{1}{\text{Pa}}.$$

In the present formulation a big part of the behaviour of the model is governed by the interplay between water transport at the macro level and water transport from the macro to the micro level. With the described formulation, the first process can easily be adjusted trough $fact_\kappa$ and the second through $fact_\alpha$. In the most recent setup, the values

$$fact_\kappa = 1 \cdot 10^{-5},$$

$$fact_\alpha = 1.7 \cdot 10^{-3},$$

have been used. It could however be that both multiplicators could be changed from these values without a dramatic change in the behaviour of the model, since it seems to be the relation between the two water transport processes that is important, not necessarily the magnitude of the multiplicators.

2.4 Piping channel formation

The algorithm used to determine if and where a piping channel should be created is described in this section. A piping channel was created if the macroscopic pore pressure, $-s_M$, was above a prescribed limit, $-s_M > p_{piping}$, where $p_{piping} = 15$ kPa has been used. The pressure condition was only investigated in a limited subset of the geometry. The subset was chosen as being the vicinity of the endpoint of the last formed channel part. This was defined by a local radius, r_p, at the channel endpoint. Additionally, the condition was formulated as to investigate the *maximum pressure within the endpoint vicinity*, i.e. the condition $\max\left(-s_M(X)\right) > p_{piping}$ was investigated when $r(X) < r_p$.

If the condition described above was fulfilled in point X_p, an elliptic channel section was formed with X_p at a focal point, see Figure 2-3. The orientation of the new channel section was in the direction of the macroscopic suction gradient $\nabla s_M / |\nabla s_M|$ at X_p. In the algorithm, the state variable, $pipe$, with the initial condition 0, was set to 1 if a point X belonged to a pipe channel. In the presented realizations the elliptic pipe channel was specified to have length $2a_p = 10$ cm, width $2b_p = 2$ cm and the local radius r_p, defining the vicinity of the channel endpoint where the pressure condition was evaluated, was chosen as $r_p = b_p$.

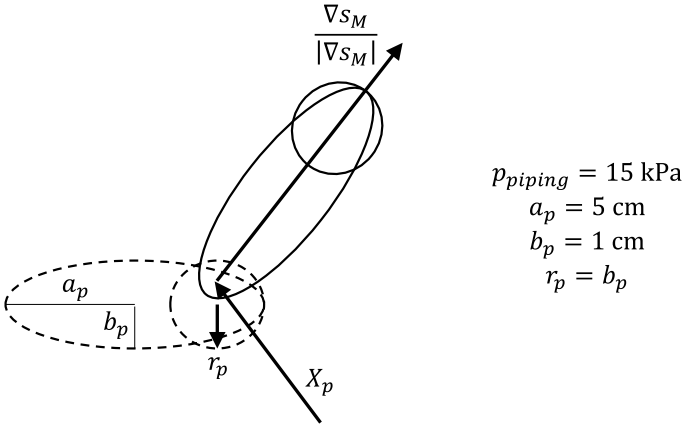

Figure 2-3. Geometry of the piping channel section and the pipe formation parameters.

3 Implementation in Comsol Multiphysics

The implementation of the water mass balance in the Comsol Multiphysics framework is described below. The description is more general than the implementation used in this work, the densities are assumed dependent on the corresponding suction variable, and there is non-zero Darcy flow assumed at the micro scale. The water mass balance equations, written separately on micro and macro scales, read,

$$(1-\phi)\,\dot{\overline{{}^{\mu}\rho_l e_\mu}} + \operatorname{div}\left({}^{\mu}\rho_l\,{}^{\mu}\boldsymbol{q}_l\right) = {}^{\mu}f_l^{w}\,,$$

and

$$(1-\phi)\,\dot{\overline{{}^{M}\rho_l\,{}^{M}S_l e_M(1+e_m)(1+e_\mu)}} + \operatorname{div}\left({}^{M}\rho_l\,{}^{M}\boldsymbol{q}_l\right) = {}^{M}f_l^{w},$$

respectively.

In Comsol Multiphysics there is an option of using a general form PDE which reads,

$$\boldsymbol{e}_a\frac{\partial^2\boldsymbol{u}}{\partial t^2} + \boldsymbol{d}_a\frac{\partial\boldsymbol{u}}{\partial t} + \nabla\cdot\boldsymbol{\Gamma} = \boldsymbol{f}.$$

The independent variables for which the water balances are solved for are micro and macro suction, s_μ and s_M, respectively, i.e. $\boldsymbol{u} = [s_\mu\ s_M]^{\mathrm{T}}$. Since there are no second orders derivatives in the mass balances $\boldsymbol{e}_a = \boldsymbol{0}$. The second order coefficient matrix $\boldsymbol{d}_a$ has the elements,

$$d_{a_{11}} = (1-\phi)\left(\frac{\partial\,{}^{\mu}\rho_l}{\partial s_\mu}e_\mu + -{}^{\mu}\rho_l\frac{\partial e_\mu}{\partial s_\mu}\right)$$

$$d_{a_{12}} = 0$$

$$d_{a_{21}} = (1-\phi)\,{}^{M}\rho_l\,{}^{M}S_l\left(\frac{\partial e_M}{\partial e_\mu}(1+e_m)(1+e_\mu) + e_M\frac{\partial e_m}{\partial e_\mu}(1+e_\mu) + e_M(1+e_m)\right)\frac{\partial e_\mu}{\partial s_\mu}$$

$$d_{a_{22}} = (1-\phi)e_M(1+e_m)(1+e_\mu)\left(\frac{\partial^M\rho_l}{\partial s_M}{}^{M}S_l + {}^{M}\rho_l\frac{\partial^M S_l}{\partial s_M}\right)$$

The "flux vector" $\boldsymbol{\Gamma}$ is defined by,

$$\boldsymbol{\Gamma} = \begin{bmatrix} {}^{\mu}\rho_l\,{}^{\mu}\boldsymbol{q}_l \\ {}^{M}\rho_l\,{}^{M}\boldsymbol{q}_l \end{bmatrix},$$

and the final part is the "source vector" $\boldsymbol{f}$ defined by,

$$\boldsymbol{f} = \begin{bmatrix} {}^{\mu}f_l^{w} \\ {}^{M}f_l^{w} \end{bmatrix}.$$

4 Test simulation 1

In this study the piping channel formation logic was investigated. To do this a test simulation was carried out using $fact_\kappa = 5 \cdot 10^{-9}$ which promoted the channel formation in the model and also provided numerically stable conditions.

The test simulation had a plane four-sided geometry with side length of 1 meter, and water inflow took place along an internal circular boundary with radius 5 mm, centred in the geometry, see Figure 4-1. An inflow rate of 0.01 l/min was used. No-flow conditions were prescribed along the outer boundaries.

Since the model use a plane assumption, sections perpendicular to the out of plane axis are identical and all inflow rates should be viewed as being prescribed per m along the out of plane dimension. So, just for clarity, the inflow rate specified above should be interpreted as being 0.01 l/min/m. This will however not be written out in the following.

The initial conditions used in the model is given by: $\rho_s = 2780$ kg/m^3, ${\rho_d}^0 = 1000$ kg/m^3, ${\rho_{d\_pellets}}^0 = 1841$ kg/m^3, $w^0 = 0.125$, ${s_M}^0 =$ -200 Pa, ${s_\mu}^0 = 63.33$ MPa (given by the micro retention relation).

The following was used to calculate the initial void ratios:

$$e^0 = \frac{\rho_s}{{\rho_d}^0} - 1,$$

$${e_M}^0 = \frac{{\rho_{d_{pellets}}}^0}{{\rho_d}^0} - 1,$$

$${e_m}^0 = \frac{\rho_s}{{\rho_{d_{pellets}}}^0\left(1 - {e_\mu}^0\right)} - 1,$$

$${e_\mu}^0 = \frac{\rho_s}{\rho_l} w^0 .$$

In Figure 4-2 a sequence of results, the total saturation and pipe state variable, is shown. The saturation pattern follows the pipe state variable which starts about 45° from the horizontal axis and then turns towards being vertical.

Table 4-1 Model identification.

Test 1 Simulation	Pellets_OKr_07C_original

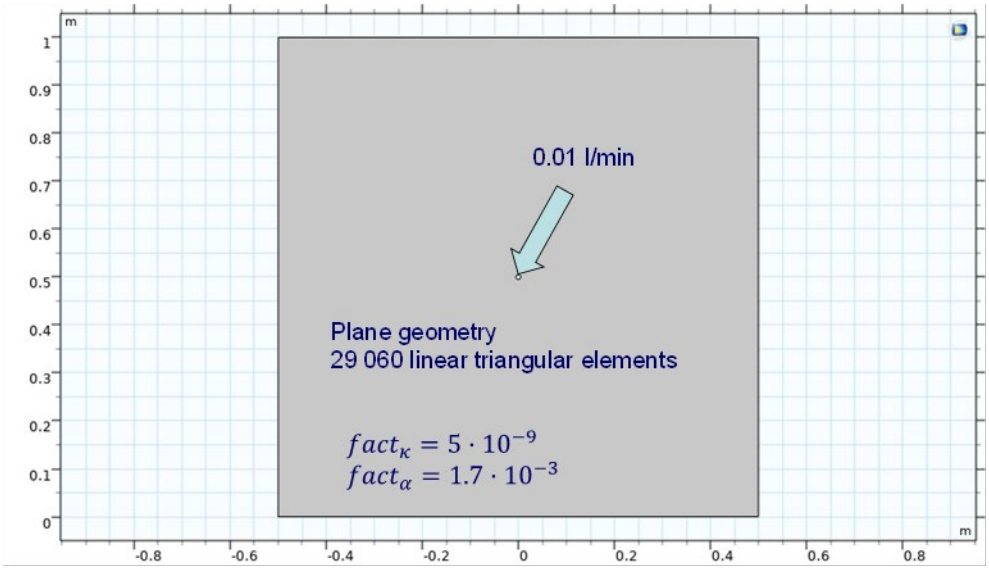

Figure 4-1. Geometry, and model setup for the piping channel formation test.

The reason for the initial asymmetric direction with respect to the vertical plane through the centre of the geometry could be that there are asymmetries in the numerical representation, for instance using an asymmetric mesh. When using a finer mesh, however, the channel path was not significantly changed.

To check that the channel formation is working the results in Figure 4-3 can be studied. Figure 4-3 shows the maximum pore pressure in the piping channel end zone, normalized using the piping pressure parameter of 15 kPa. Below the graph a sequence of the pipe state variable at 10 h, 30 h, and 80 h is shown. The graph shows that a channel section is formed almost instantly after the model is started, i.e. the normalized pressure increases to 1 very early. Thereafter the pressure decreases when the permeable channel section becomes water saturated and after this the pressure starts to increase again. This is the condition after 10 h in the model and the pipe state variable corresponds to this, one channel section has been created. If studying the "snapshots" at 30 h and 80 h, 2 and 4 channel sections have been created, respectively, which agrees with the number of times the normalised pressure in the graph has passed the value one.

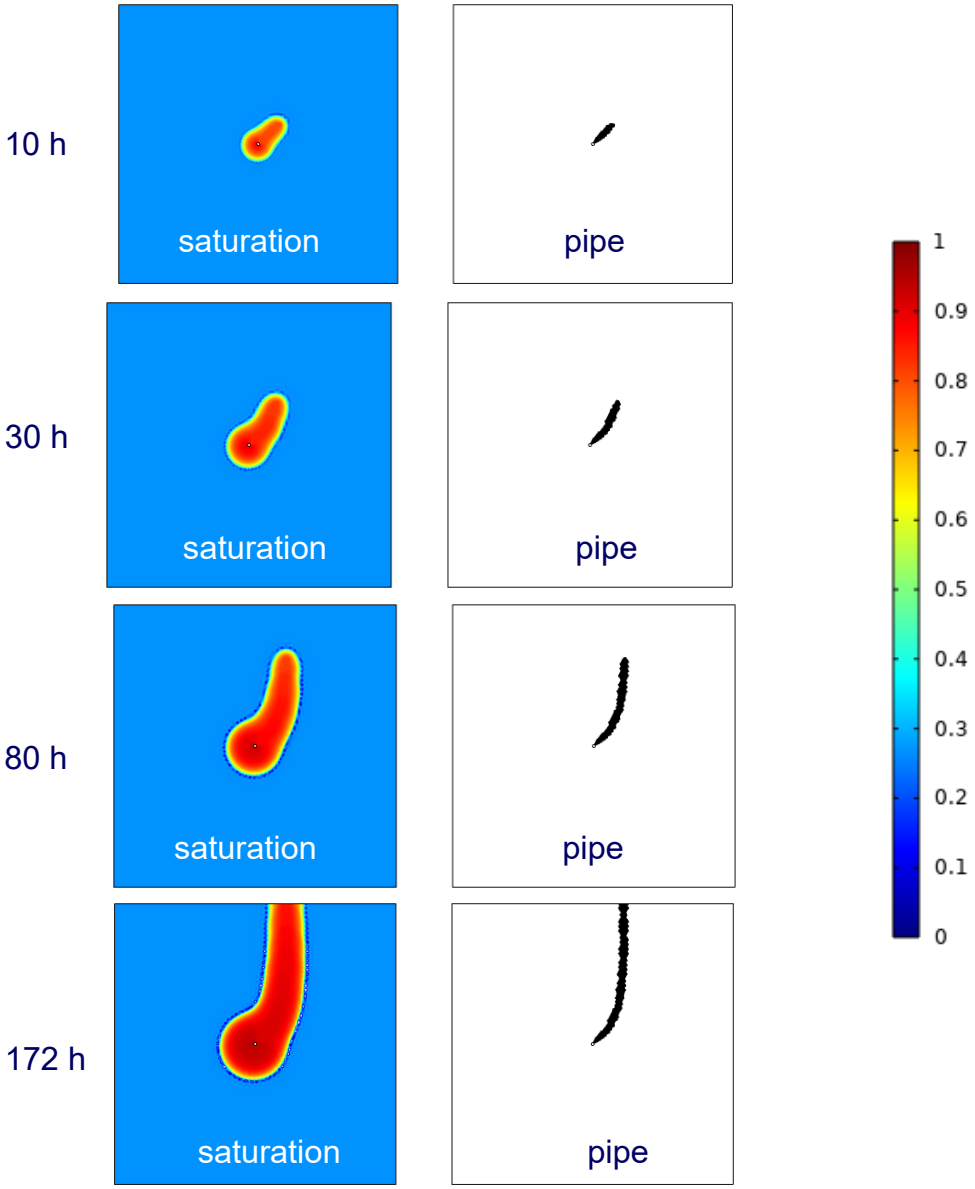

Figure 4-2. Sequence of total saturation and pipe state variable in the piping channel formation test.

To test the pipe formation further, another model was carried out where the direction of gravity was reversed, now acting “upwards”. This model did not, however, as expected produce a channel directed downwards. The channel instead continued to the side. This indicate that something is either incorrect or unsuitable with the piping formation in the present version. The suspected part in the formulation/implementation is where the orientation of a new channel segment is determined. The asymmetric start of the channel in the model with gravity oriented downwards could also be an indication of something improper with the channel formation and not just a consequence of numerical asymmetries.

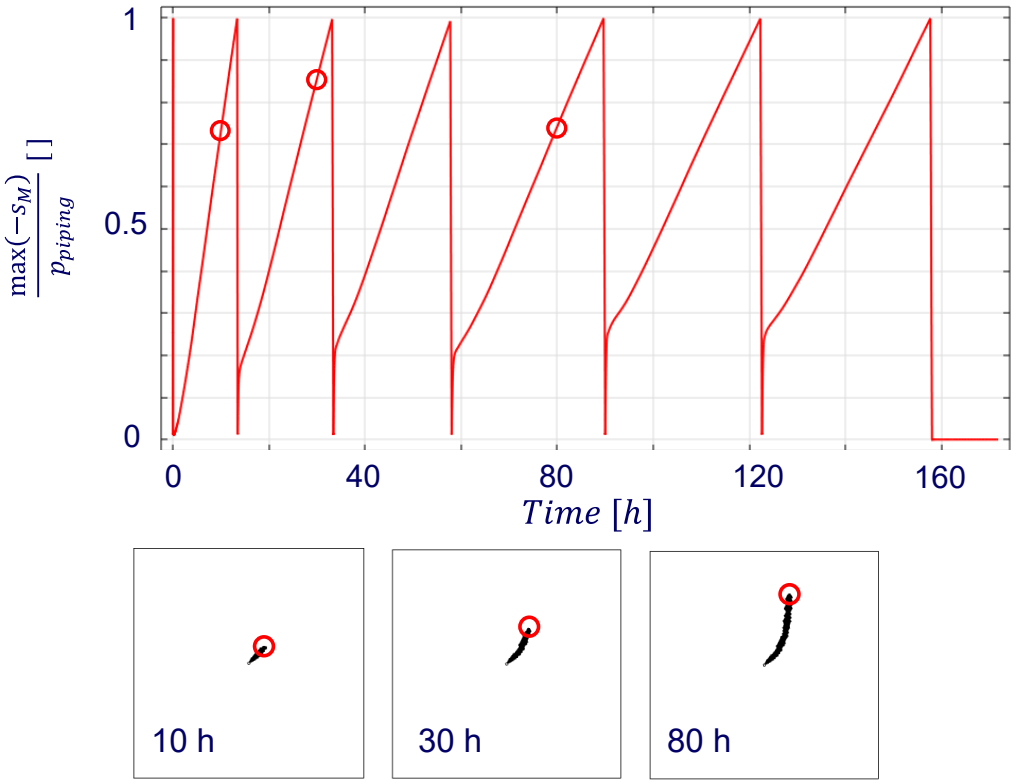

Figure 4-3. Maximum pore pressure in the channel end zone normalized with the piping pressure (top). Sequence of pipe state variable at 10 h, 30 h and 80 h (bottom).

5 Test simulation 2

To test the water transport model further, a similar test setup as described above was evaluated using three different point inflow rates, 0.1 l/min, 0.01 l/min and 0.001 l/min. The models were identical to what was described in test simulation 1 except for the inflow rates and the initial micro suction. As in the previous modelling all inflow rates should be viewed as being prescribed per m along the out of plane dimension. The intention was to use the same initial micro suction as before, but a specified micro suction was unknowingly remaining from another model setup which gave 63.50 MPa instead of 63.33 MPa.

The purpose of this study was to see if changes in the water inflow rate led to a change in the water saturation mode according to that observed in experiments, some reported in Börgesson et al. (2015). In the same report a conceptual model was developed where the saturation pattern was specified as being, downwards, centred, and upwards, for 0.1 l/min, 0.01 l/min and 0.001 l/min, respectively.

As before, the test simulation had a plane four-sided geometry with side length 1m, and the water inflow took place along an internal circular boundary with radius 5 mm, which was centred in the geometry, see Figure 5-1. No-flow conditions were used at the outer boundaries. The models simulated the saturation until 20% of the initially available pore volume was water filled. The duration of the water inflow, $\Delta t = t_{20\%}$ was, 8.59 h, 85.9 h and 859 h for inflow rates, 0.1 l/min, 0.01 l/min and 0.001 l/min, respectively.

The initial conditions were identical to those used in test simulation 1 except for the micro suction as explained in the first paragraph.

In Figure 5-2 evolution of the total saturation for the three different inflow cases are shown at three different times. The results of the two higher inflow rates agree well with the modes in saturation pattern observed in experiments. For the case where the inflow rate was 0.1 l/min, the saturation pattern is directed downwards from the inflow point. With an inflow rate of 0.01 l/min, the saturation pattern is centred around the inflow point.

Table 5-1 Model identification.

Test 2 Simulation, 0.1 l/min	Pellets_OKr_07D_01
Test 2 Simulation, 0.01 l/min	Pellets_OKr_07D_001
Test 2 Simulation, 0.001 l/min	Pellets_OKr_07D_0001

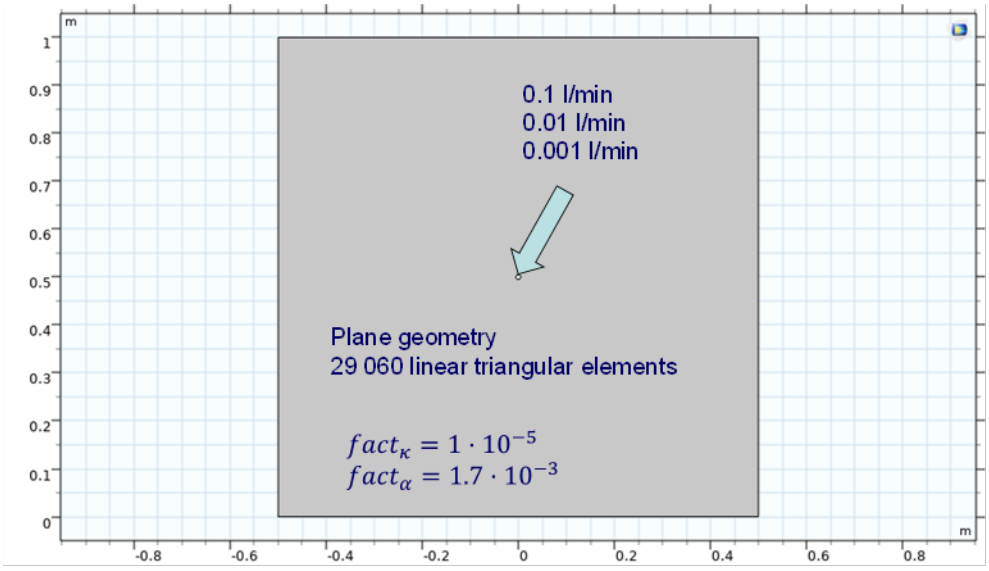

Figure 5-1. Geometry, and model setup for the saturation mode test.

When simulating the case of 0.001 l/min, the saturation pattern also looks centred around the inflow point, but more concentrated as compared to the solution when using 0.01 l/min. This goes somewhat against what has been observed in experiments where saturation patterns were directed upwards from the inflow point. The simulation of the low inflow case crashed just before reaching half the simulation time, so it should be noted that the iso maps shown in the lower row of Figure 5-2 cannot be directly compared with the ones above.

If studying the solution of the low inflow case in more detail, see Figure 5-3 and Figure 5-4, it can be seen that the channel formation has started. The pore pressure evolution about at the channel end shows that three channel segments have formed when the simulation crashes. This shows that the "piping mode" has been activated which could enable a saturation pattern directed upwards.

It should however be stressed that the "reversed gravity" test case, described at the end of the "Test simulation 1" section, indicates that there is something improper with the current formulation in how the channel direction is determined. This needs to be addressed before a full assessment of the formulation can be carried out.

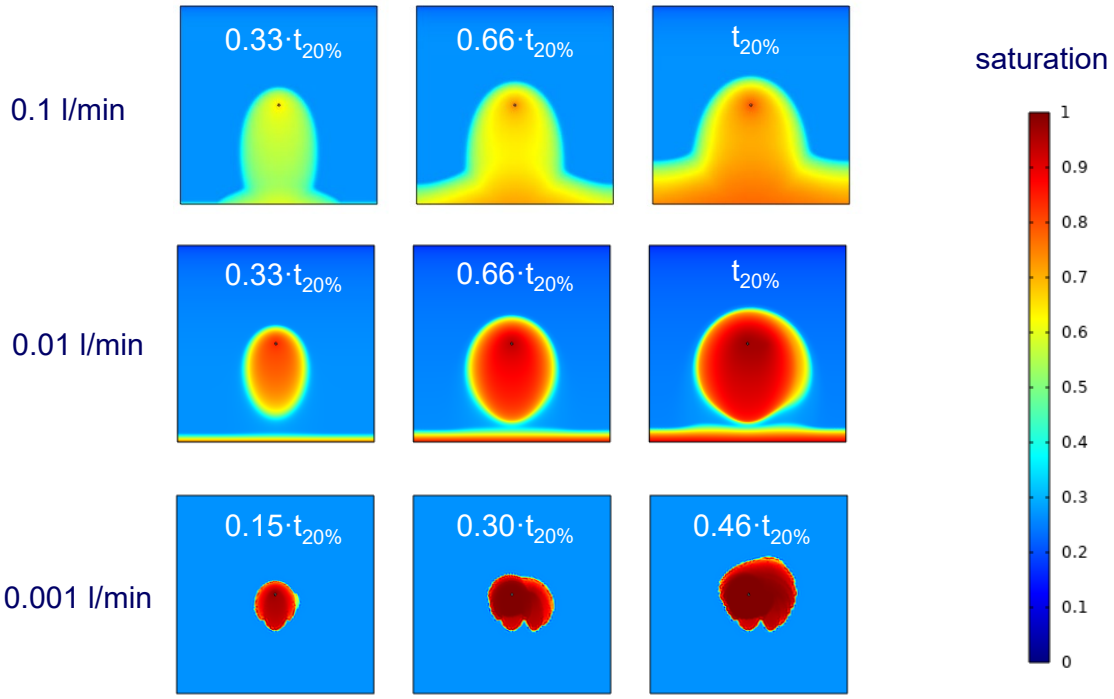

Figure 5-2. Sequences of total saturation for 0.1 l/min, 0.01 l/min and 0.001 l/min. The 0.001 l/min simulation crashed at 0.46·t20%, that is why the results are shown for different relative times.

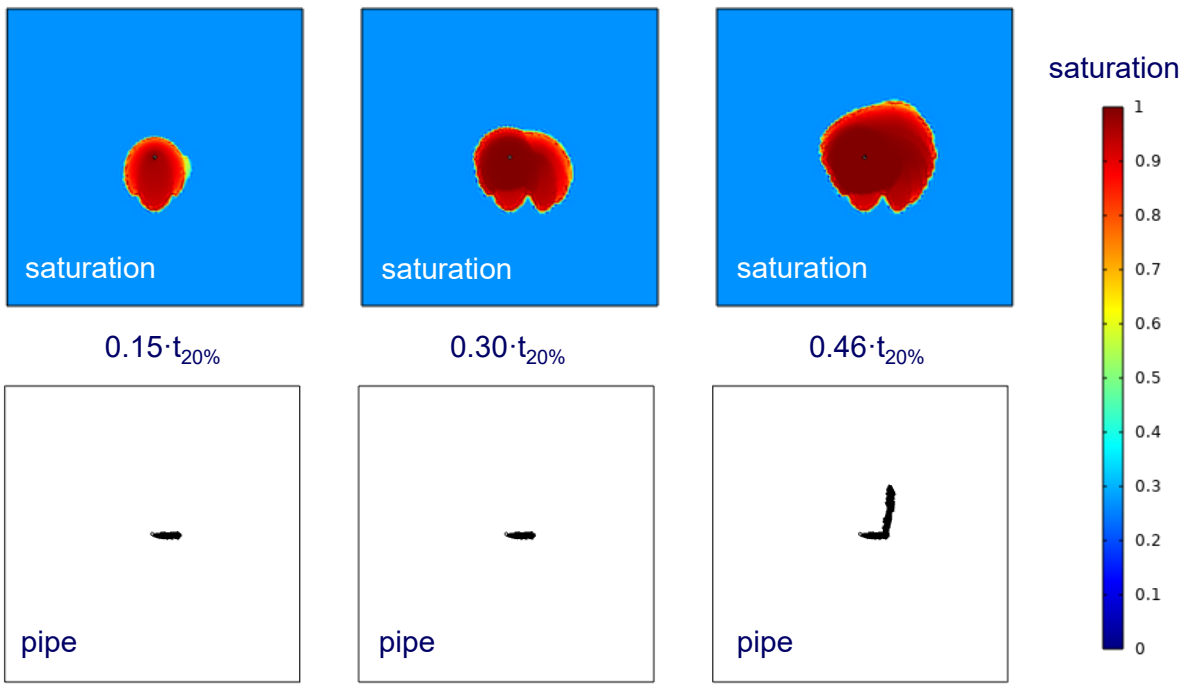

Figure 5-3. Results from the 0.001 l/min simulation. Sequences of total saturation (top) and pipe state variable (bottom) at 129 h, 258 h and 399 h.

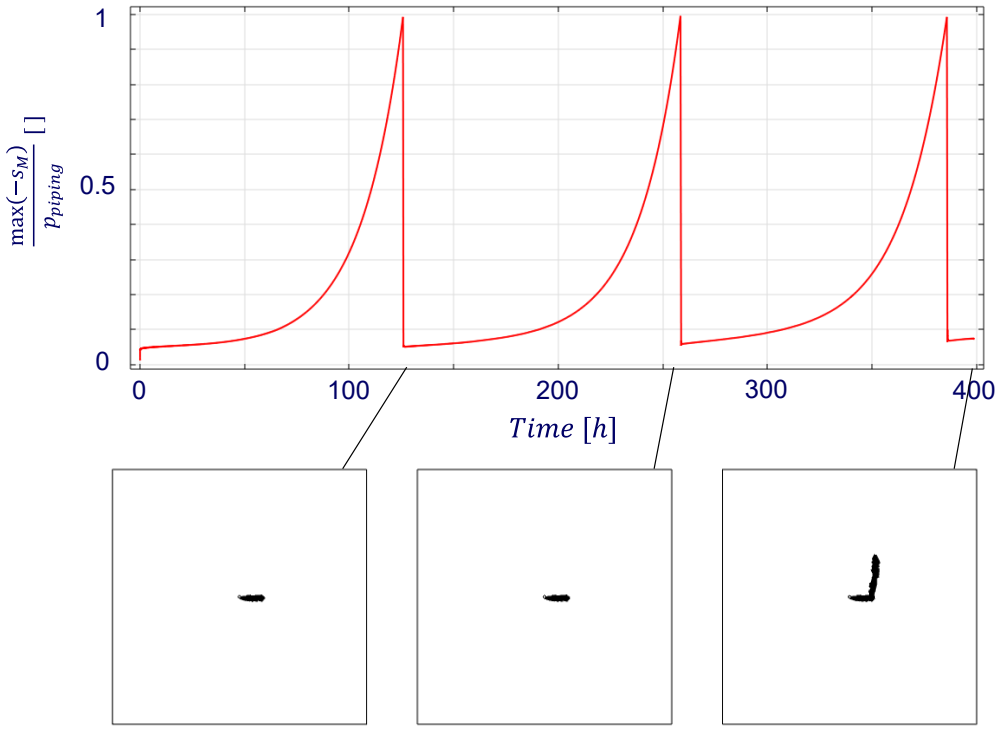

Figure 5-4. Results from the 0.001 l/min simulation. Maximum pore pressure in the channel end zone normalized with the piping pressure (top). Sequence of pipe state variable at 129 h, 258 h and 399 h (bottom).

6 Conclusions and comments

- The channel formation algorithm is working. The way the direction of new pipe segments is determined, however, seems to be improper.
- The formulation can capture different wetting modes for different inflow rates. The behaviour corresponds rather well with experimental data, more so for high inflow rates due to the improper piping formation which becomes more influential at lower inflow rates.
- Further work on this material model could include:
  - Debugging/reformulating the part where the channel orientation is determined.
  - Treatment of convergence issues for slow inflow rates which seem to stem from negative macro saturation.
  - Testing alternative ways to “restrain” the model as not to produce negative macro saturation.
  - Trying to address the problem with negative saturation directly by designing a new macro retention curve.
  - There might also be better combinations of the controlling multiplicators $fact_{\kappa}$ & $fact_{\alpha}$ which could be further evaluated both theoretically and numerically.

References

SKB's (Svensk Kärnbränslehantering AB) publications can be found at www.skb.com/publications.

Börgesson L, Sandén T, Dueck A, Andersson L, Jensen V, Nilsson U, Olsson S, Åkesson M, Kristensson O, Svensson U, 2015. Consequences of water inflow and early water uptake in deposition holes. EVA project. SKB TR-14-22, Svensk Kärnbränslehantering AB.

Eriksson P, 2020. Effects of water inflow to deposition hole during the installation phase. SKB R-20-07, Svensk Kärnbränslehantering AB.

Kristensson O, Åkesson M, Malmberg D, Spetz A, 2021. Annex C in Beacon D3.3: Description of the constitutive models developed in the project. Conceptual bases, mathematical description and model capabilities. Assessment of predictive power. BEACON.